Cloud Publications
International Journal of Advanced Remote Sensing and GIS
2016, Volume 5, Issue 6, pp. 1768-1786
ISSN 2320 - 0243, Crossref: 10.23953/cloud.ijarsg.59

Research Article | Open Access

Analysis of the Fitting Accuracy of the 3d Affine Transformation Applied to Cartosat-1 (IRS P5) Satellite Stereo Imagery

Farzaneh Dadras Javan and Ali Azizi

Dept. of Photogrammetry, Faculty of Geomatics, University College of Engineering, University of Tehran, Iran

Publication Date: 27 June 2016

DOI: https://doi.org/10.23953/cloud.ijarsg.59

Abstract Since few years ago it has been generally accepted without any dispute that the 3D affine transformation applied to high-resolution satellite imageries (HRSI), produces results as accurate as those obtained by the RPCs derived from rigorous photogrammetric model. However, as the higher order terms are absent in the affine transformation, the degree of success of this model obviously hinges upon the geometric nature of the imagery to be geo-rectified. In authors view, there are a latent confusion and misunderstanding in the minds of the photogrammetric practitioners as regards the potential of the 3D affine transformation as a replacement model for the geometric correction of the HRSI. The main intention of this paper is, therefore, to analyse the 3D affine transformation by concentrating more on its limitations. To obtain deeper insight into the nature of the 3D affine model, it is applied to images with larger field of view as well as the images of highly mountainous terrains. The geo-coding success of the affine model is then evaluated by comparing the object coordinates of a dense cloud of homologous points derived by the affine model with the object coordinates of the same points obtained by the standard terrain-independent rational functions. Extensive tests conducted over excessively mountainous as well as the hilly terrains indicate that there are clear distortion trends in the residual ground coordinates that cannot be fully absorbed into the 3D affine coefficients. The sources of these non-linear trends such as the satellite attitude and position variations, the terrain relief, the earth curvature and their impact on the final accuracy are analysed using the scatter patterns of the residual errors.

Keywords *3D Affine Transformation; High Resolution Satellite Imagery; Cartosat-1; Rational Polynomial Functions; RPCs; Geometric Accuracy; Perspective to Affine Transformation; Parallel Projection*

1. Introduction

In recent years, the major trends in sensor orientation and geo-positioning solutions for high resolution satellite imageries have been dominantly confined to the fitting rational function coefficients to the rigorous photogrammetric collinearity equations (Tao et al., 2001; Dial and Grodecki, 2005; Grodecki, 2001). This approach proved to be accurate, flexible and easy to implement and hence the main stream photogrammetric software developers did not hesitate to tailor the RPC-based 3D ground reconstruction into their systems.

The suitability of RPC approach can be justified based on the following reasons:

1) The on-board GPS/INS-star tracker facilities provide precise attitude and satellite position data to serve as observational data for the exterior orientation parameters in collinearity model leading to direct-geo positioning (Grodecki and Dial, 2003),
2) Decades of research proved the excellence of the Collinearity Equation for rigorously modelling the geometry of the satellite linear array imaging systems (Valadan Zoej and Petrie,1998),
3) After bias and drift is removed, the fitted RPCs are effectively as accurate as the collinearity model itself (Grodecki and Dial, 2003; Fraser and Hanly, 2003),
4) The problematic bias and drift parameters are easily tackled by a very few GCPs (Grodecki and Dial, 2003; Fraser and Hanly, 2003; Hanley and Fraser, 2004),
5) 3D ground reconstruction with RPCs is easy to implement with well-established formulations (Grodecki et al., 2004),
6) The user may easily develop his own bundle adjustment to calculate the object coordinates,
7) The manual 3D displacements of the floating mark in Photogrammetric work stations can be controlled via the fitted RPCs.

On the other hand, there has been a second main stream research trends that chose to go on different direction, and that is the famous 3D affine projection model initially suggested by Okamoto (Okamoto et al., 1998). This approach also indicated to be attractive in its simplicity and its outstanding potential to give “accuracies equal to and in cases superior to those obtained via the RPC approach” (Fraser and Yamakawa, 2004). The affine projection offers the following advantages:

1) Easy to implement,
2) No initial values are required for the solution of the affine transformation coefficients and the ground coordinates,
3) The solution is non-iterative,
4) No oscillation and collapsing occurs in the equation,
5) Normalization and regularization are not essential,
6) Few GCPs are needed to solve the sensor orientation.

Now, bearing in mind the reported accuracy figures obtained by the simple 3D affine projection approach (Fraser and Yamakawa, 2004; Elashmawy et al., 2005; Willneff et al., 2008), one could logically conclude that the eight coefficients of the 3D affine transformation are effectively equivalent to the 80 RPCs in the rational function model, i.e. the geometric non-linearities of the HRSIs under the test are negligible. This, obviously, has no mathematical justification. If, on the other hand, there are some distortion patterns that cannot be perfectly eliminated by the affine transformation, then what are those influential factors that the affine transformation fails to eliminate and in which situations this transformation can produce compatible results with the RPC approach?

To answerer these questions, it is necessary to expose the affine transformation to the situations in which significant higher order distortions in the images are available. In the present research project, this is achieved by using the Cartosat-1 (IRS-P5) satellite image which has larger FOV compared to the other existing HRSIs. Moreover, the P5 stereo images used in this project are taken over a terrain with very high relief variations leading to the corresponding high relief displacements. To be able to determine the rate of success of the affine transformation, it is of crucial importance not to rely solely on RMSE’s and the min/max of the residual errors.

The reason for this is that, depending on the number and distribution of the GCPs and bearing in mind the fact that the error patterns may be symmetrical; the resulted accuracy figures could be misleading.

Instead, in this project, the accuracy evaluation has been conducted using point clouds with regular distribution over the entire image plane. In this way, it has been possible to realistically analyse the rate of success of the affine projection model and its limitations using the scatter patterns of the residual errors for the point clouds.

To establish a firm theoretical basis for further analysis, the first section of this report derives the 3D affine transformation based on the parallel projection theorem. The 3D affine is then diagnosed in some detail to clarify the problems and limitations associated with this transformation as applied to the HRSIs. After a short introduction to the main characteristics of the Cartosat-1 (IRS-P5) images, different sources that generate higher order distortion patterns in these images are identified and analysed. These are then followed by detailed examination of the significance of these nonlinear terms using several tests carried out on Cartosat-1 toolkit stereo imageries.

1.1. Rigorous Parallel Projection and 3d Affine Transformation

The mathematical formulation for the rigorous parallel projection has been thoroughly discussed by Morgan (Morgan, 2004). It can be briefly stated as follows: With reference to Figure 1, it is assumed that the points in the image space are formed by the projecting rays that are parallel, i.e. the projection centre lies at infinity. This projective geometry, obviously, differs from the customary perspective projection in which the projecting rays converge to a point located at a finite distance. For parallel projection geometry, similar to the perspective geometry, it is possible to derive a rigorous mathematical model. Consider the image point a' and its corresponding point A on the ground, the rigorous parallel projection is then given by (details are given in Morgan, 2004):

$$\begin{pmatrix} x' \\ y' \\ 0 \end{pmatrix} = S\left(\lambda \bullet R \begin{bmatrix} L \\ M \\ N \end{bmatrix} + R \begin{bmatrix} E_A \\ N_A \\ h_A \end{bmatrix} \right) + \begin{pmatrix} \Delta x \\ \Delta y \\ 0 \end{pmatrix} \qquad (1)$$

where, *x'*, *y'* are the image coordinates; *L*, *M*, *N* are the three components of the unit direction vector; *R* is the scene rotation matrix; *S* is the scale factor; E_A, N_A, h_A are the object coordinates of the point *A;* Δx , Δy are the shifts in image space and λ is the distance between the object point and its corresponding image point.

Now, if λ is eliminated and under the constant velocity and constant attitude (CVCA) assumption, Equation 1 reduces to the familiar form of the 3D affine transformation, i.e.

$$\begin{aligned} x' &= A_1E + A_2N + A_3h + A_4 \\ y' &= A_5E + A_6N + A_7h + A_8 \end{aligned} \qquad (2)$$

where, x', y' are the pixel coordinates; E, N, h are the object coordinates and Ai are the 3D affine transformation coefficients. Similar pair of equations may be obtained for the corresponding right image points leading to four 3D affine equations for each homologous point. It should be noted that, the 3D affine transformation may be regarded as the parametric form of the rigorous parallel projection, if and only if the following conditions are fulfilled:

- *E*, *N* plane is not curved;
- The rays are parallel, i.e. the projection centre is at infinity;
- Satellite moves with constant velocity and constant attitude.

If any of the aforementioned conditions are not satisfied, the affine transformation cannot represent faithfully the parallel projection model. The section that follows lists and discusses the factors that influence the fidelity of the affine model.

1.2. Geometric Limitations of the 3d Affine Transformation

(A) *General Considerations*

There are certain well known factors that violate the parallel nature of the affine transformation. These are:

(1) Internal errors of the CCD lines: These are mainly, CCD scan line rotation and bending in focal plane, lens distortion, principal point displacement and scale variation in scan and line directions respectively. These errors are taken into account in the collinearity equations and subsequently are catered for in the rational RPCs but are normally ignored in the 3D affine transformation.
(2) Height variations in the scan direction (i.e. linear array direction) are projected according to the central perspective geometry and therefore the perspective to parallel transformation (PTP) is required (Okamoto et al., 1998; Fraser and Yamakawa, 2004; Morgan et al., 2004).
(3) Scan line rotation around the z axis (yaw rotation) introduces an effect similar to the CCD rotation in the focal plane.
(4) The vertical line passing through the projection centre does not remain parallel from one scan line to the other because of the curvature of the satellite route.
(5) Map projection used for the object coordinates, introduces additional non-linear distortions.
(6) As discussed before, the 3D affine transformation rigorously models the parallel projection geometry under the restrict proviso of CVCA condition. Any deviation in the satellite route and any attitude variations disturb the parallel projection requirements.

(B) *Earth Curvature Considerations*

The earth curvature, normally, does not conform to the nature of the 3D affine transformation. This is due to the fact that a curved surface mapped into a 2D image plane, inevitably imposes distortions on this plane. With the physical 3D reconstruction models, however, this distortion does not pose a difficulty. This is because the original pair of image forming incoming rays, irrespective of the complexities associated with the object surface, are regenerated in a reverse mode to reconstruct the object points. Therefore, with a selection of an appropriate object coordinate system, the planar image plane can be re-projected into a curved object surface without any significant distortion. However, the affine transformation is not flexible enough to perform similar task. In other words, the affine transformation, which is parametric and not physical, maps a 2-D space into a 3D space with 8 parameters with a property that a curve with a given degree is transformed into another curve with the same degree. That is, the mapped object surface must hold true in a plane given by:

$$AX + BY + CZ + D = 0.$$

This indicates that there are limitations inherent in the 3D affine transformation if the object space is a curved surface. This fact is demonstrated in Figure 1. As the Figure indicates, assuming no height variation, each scan line inevitably maps a curved surface. From this, it can be deduced that the points with the same height values are not mapped into the same scan line and therefore effectively different x-parallaxes are introduced to the points with the equal heights leading to the height distortion on the generated object space. Distortions in the regenerated planimetric coordinate of the object points also occur but with a smaller rate.

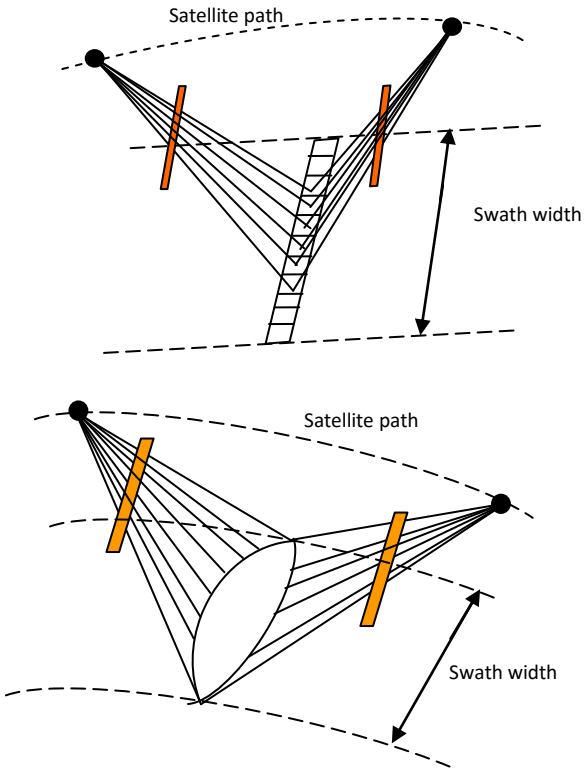

Figure 1: *Image geometry for a flat surface (above) and a curved surface (below)*

2. Accuracy Evaluation Strategy

The current approaches for accuracy assessment of the generated 3D points in object space for satellite imageries generally rely on the control and check points that are identified on the HRSI and measured on the ground using GPS or other geodetic surveying techniques. Alternatively, the GCPs may be identified and measured using existing maps. These approaches, however, suffer from certain ambiguities and uncertainties that result from the fact that the imaging system's point spread function smoothes the well-defined points. Hence ambiguity occurs during the point measurement process. Correlatively, the corresponding ground point identification undergoes the same ambiguities and the object point positioning uncertainties become inevitable. Moreover, due to the nature of the ground and other prohibiting factors, it is not always possible to extend the measurement to cover the entire area with uniform distribution of the points. This in turn weakens the accuracy assessment outcomes. To avoid these ambiguities in accuracy assessment and to reach a definite conclusion as regards the accuracy figures, this research adopts a fitting approach based on the procedures given in Figure 2.

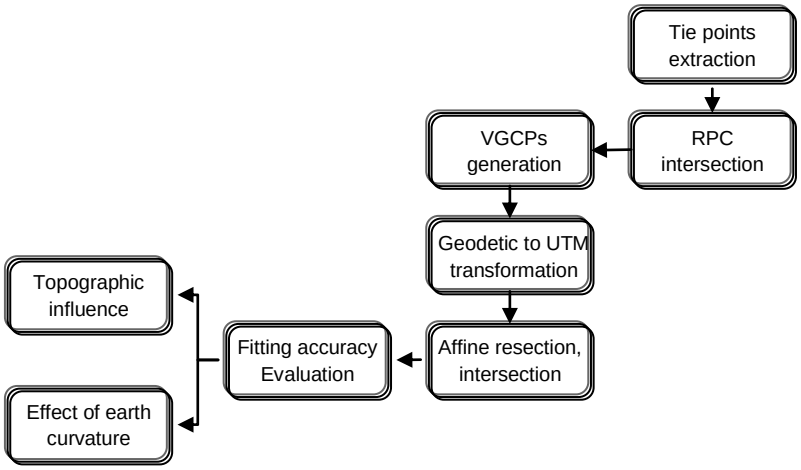

Figure 2: *Accuracy evaluation strategy*

As the Figure indicates, the procedure starts by measuring well distributed arbitrarily chosen homologous point clouds covering the entire stereo pair overlap area. The measurements are performed both manually and automatically. Both of the manual and automatic homologues point measurements can be performed with sub-pixel accuracy (see the section: "*preliminary data analysis"*). Using the available RPCs, the object space coordinates are then calculated by adopting the well-established RPC object point reconstruction formulation given by the following linearized rational equations: Grodecki et al., 2004,

$$s = s_O + s_s \begin{pmatrix} \frac{\partial K}{\partial X} & \frac{\partial K}{\partial Y} & \frac{\partial K}{\partial Z} \end{pmatrix} \begin{pmatrix} \frac{1}{\varphi_s} & 0 & 0 \\ 0 & \frac{1}{\lambda_s} & 0 \\ 0 & 0 & \frac{1}{h_s} \end{pmatrix} \begin{pmatrix} d\varphi \\ d\lambda \\ dh \end{pmatrix}$$

$$l = l_O + l_s \begin{pmatrix} \frac{\partial J}{\partial X} & \frac{\partial J}{\partial Y} & \frac{\partial J}{\partial Z} \end{pmatrix} \begin{pmatrix} \frac{1}{\varphi_s} & 0 & 0 \\ 0 & \frac{1}{\lambda_s} & 0 \\ 0 & 0 & \frac{1}{h_s} \end{pmatrix} \begin{pmatrix} d\varphi \\ d\lambda \\ dh \end{pmatrix} \quad (3)$$

where *K* and *J* denote the rational function equations respectively; *s*, *l* are the scan line and pixel coordinates; The subscripts *o* and *s* indicate the shifts and scale factors respectively used for the normalization process; the column vector comprises the unknown latitude, longitude and height differentials. Equation 3 can be written for each homologue point leading to four equations in three unknowns and solved iteratively. The generated object coordinates of the measured points provide well distributed ground points. Bearing in mind the fact that the RPCs are derived from the satellite auxiliary data by accurately fitting a rational function to the rigorous photogrammetric model, they are as accurate as the rigorous model itself. Therefore, the ground coordinates that are generated by the RPCs can be regarded as the virtual ground coordinate points (VGCPs). Consequently, these VGCPs are utilized as control points to determine the eight affine projection parameters after they have been transferred to the UTM coordinate system. This step is then followed by space intersection using all 16 affine transformation parameters determined in the previous stage. The ground coordinates for

previously measured homologous points are subsequently determined by the following linear 3D affine intersection:

$$\begin{pmatrix} x' - A_4' \\ y' - A_8' \\ x'' - A_4'' \\ y'' - A_8'' \end{pmatrix} = \begin{pmatrix} A_1' & A_2' & A_3' \\ A_5' & A_6' & A_7' \\ A_1'' & A_2'' & A_3'' \\ A_5'' & A_6'' & A_7'' \end{pmatrix} \begin{pmatrix} E \\ N \\ h \end{pmatrix} \quad (4)$$

Having calculated the object coordinates by affine intersection, it is then possible to determine the residual errors which are simply the differences between the ground coordinates of the homologous points calculated by the 3D affine and the ground coordinates of the same points determined by the RPCs, i.e.

$$\begin{pmatrix} dE \\ dN \end{pmatrix} = \begin{pmatrix} E - E' \\ N - N' \end{pmatrix} \quad (5)$$

Where *E*, …, *N'* are the calculated object coordinates by the affine and the rational functions respectively. As can be seen from the preceding discussion, it seems that there should be no ambiguity present in the analysis, because the same homologous and ground points are used for the solution of the affine coefficients. Moreover, regarding the fact that the fitted RPCs to the rigorous photogrammetric model are effectively as precise as the rigorous model, one can consider the VGCPs derived by the terrain-independent rational function, practically equivalent to the points generated by the rigorous model itself. In other words, this strategy measures the degree of the fitness of the affine transformation to the rational function model. Any remaining trend in the residual errors for the generated point clouds can also be easily observed by displaying the residual errors in a scatter diagram. Scatter diagrams are excellent means for revealing any trend in the residual errors.

2.1. Description and Analysis of the Data Sets

To be able to fully evaluate the potential of the 3D affine transformation, two sets of Cartosat-1 orthokit stereo images have been selected. These datasets belong to the areas with different topography. The first data set belongs to a highly mountainous terrain and the second data set covers a hilly area. Before describing the datasets, it seems pertinent to briefly describe the Indian Cartosat-1 satellite: It is a near polar sun synchronous satellite launched in 5 May 2005, accommodating two 2·5 meters resolution forward and afterward linear array cameras. These cameras are mounted in the satellite flight. Cartosat-1 sensor specifications are given in Table 1.

Table 1: *Geometric specifications of Cartosat-1 stereo imagery*

	Fore camera	*Aft camera*
Looking angle	+26 degree	-5 degree
Camera field of view	2·4 degree	2·4 degree
Swath width	29 km	26 km
Number of detectors	12000	12000
Focal length	1945 mm	1945 mm
Approximate altitude	618 km	618 km

Dataset (A)

The first dataset is stereo images acquired over the area of Roodehen in Iran with a range of 1345 to 3236 meters height variation for the area covered by the stereo pair. The images have been acquired

in 13 August 2007. Nearly 400 homologous points with a uniform distribution over the entire stereo-pair are measured manually. Figures 3(left) and 3(right) indicate the distribution of the homologue points measured in the fore and aft stereo images respectively.

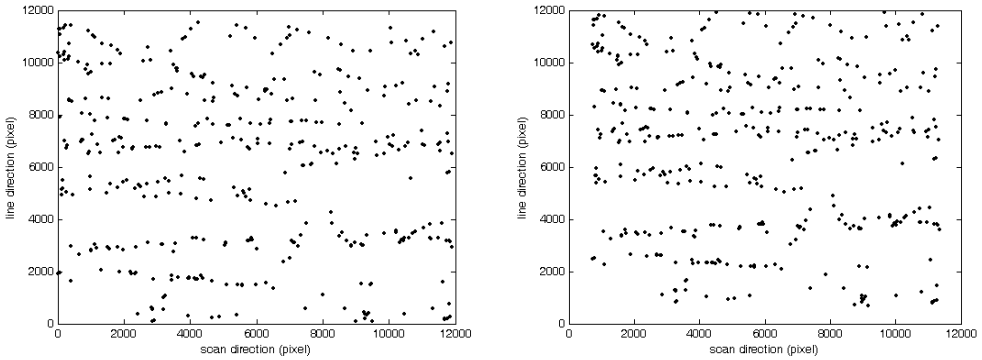

Figure 3: *Measured homologue points: (left) aft image, (right) fore image – dataset A*

For the same stereo-pair, 112 homologous points are also matched automatically using image correlation techniques. Due to the excessive height variation, the matched points were sparse and smaller in number than the manual measurements. Nevertheless, the distribution of the points was still uniform.

Dataset (B)

The second data sets are the orthokit stereo images taken over the city of Arak which is rather a hilly area with a height variation between 1624 to 1863 meters. The images have been acquired in 7 November 2006. In contrast to the first dataset in which, the automatic image matching did not succeed to produce dense homologous point cloud, in the second data set because of the smaller range of the height variations, the image matching procedures was carried out successfully and nearly 1000 homologous points were generated automatically. Figure 4 gives the distribution of the points in the fore and aft images respectively.

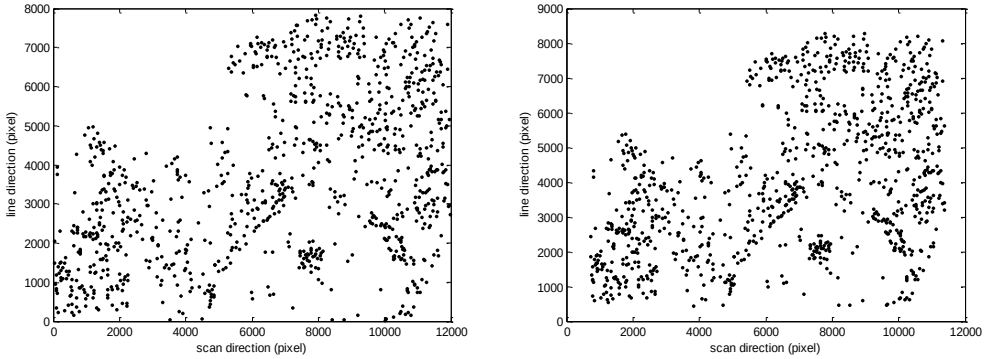

Figure 4: *Measured homologous points: (left) aft image, (right) fore image (dataset B)*

2.2. Preliminary Data Analysis

To determine a preliminary validation for the precision of the measured image points, y-parallaxes are computed based on the following relations:

$$py = p_A - p_F \qquad (6)$$

Where p_A and p_F are the pixel coordinates in the scan direction for the corresponding homologue points in aft and fore images respectively. Figure 5 (left) shows the row y-parallaxes versus line direction (i.e. satellite movement direction) for manual measurements determined by Equation 6. The linear trend in the y-parallaxes is the result of a shift and a scale factor. The shift is due to the different sample numbers for the corresponding features and the scale factor (drift) seems to be due to the scale differences in the pixel direction between the fore and aft images. After fitting a line to the raw y-parallaxes, a value of shift equal to 716 pixels and a drift equal to 0·89 is obtained. Eliminating the linear trend, the new y-parallaxes are presented in Figure 5(left). The rmse of the y-parallaxes after the removal of the linear trend is about 0·3 pixel. This indeed shows that the homologous point measurements have been performed with sub-pixel precision. The rmse for the automatically measured points is slightly smaller than the manual measurement method indicating the superiority of the automatic matching to the manual measurement approach.

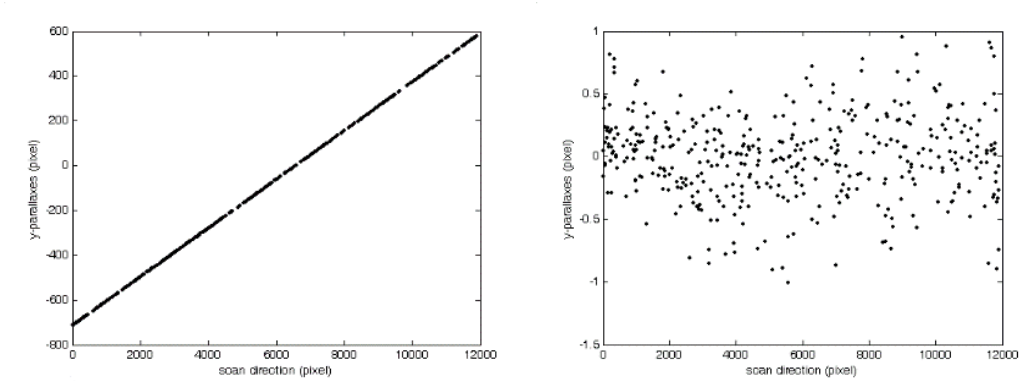

Figure 5: *Raw y-parallax versus scan direction before (left) and after linear trend is removed (dataset (A)*

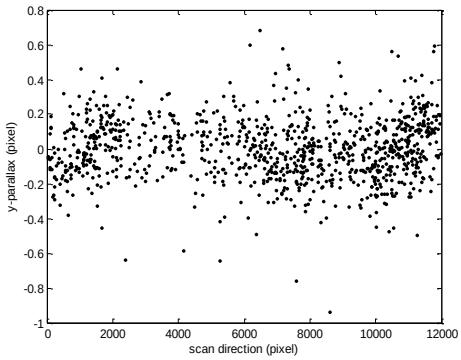

Figure 6: *y-parallax versus scan direction after the linear trend is removed (dataset B)*

Bearing in mind the fact that variations in satellite yaw, roll and pitch causes corresponding variations in y-parallaxes, the y-parallaxes can be then taken as an indication of the validity of the constant attitude assumption during the image acquisition. However, the y-parallax versus the line number indicates a very small systematic trend in the line direction (Figure 7). This small shift in y-parallaxes along the line direction (i.e. in the direction of the satellite movement) may be due to the small variations in the satellite altitude during the image acquisition (equivalent to classical *BZ*).

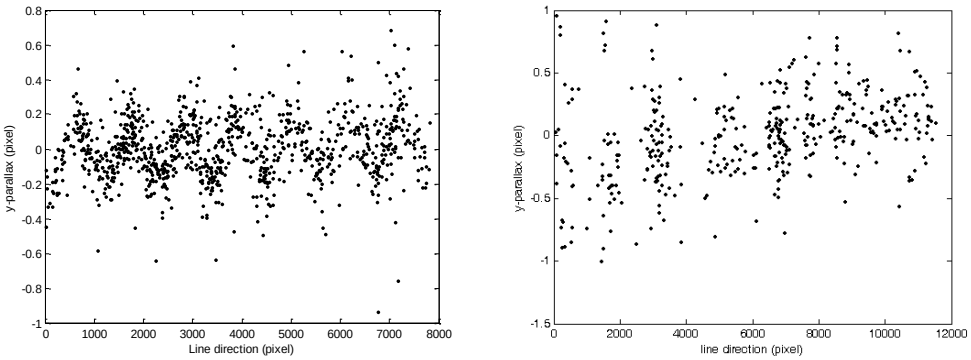

Figure 7: *(left): y-parallax versus line direction (dataset B), (right): y-parallax versus line direction (dataset A)*

3. Accuracy Results and Evaluation

Based on the strategy for the accuracy evaluation discussed in the earlier section, the first stage, with reference to Figure 2, involves calculating the object coordinates of the measured homologous points. As stated before, this stage is carried out based on the RPC intersection formulation given by Equation 3. The solution of this Equation requires initial values for the unknown 3D object coordinates. The initial values may be obtained using a truncated rational function retaining only linear terms leading to a relation similar to a simple DLT intersection. This approach is adopted and implemented with satisfactory result. However, due to the fact that during a single frame image acquisition, the CVCA condition is reasonably fulfilled (see the preceding section), our tests indicate that even very approximate initial values (e.g. the orthokit rough geodetic coordinates for the longitude and latitude and the average terrain height) can fulfil the convergence requirements (Dadrass and Azizi, 2008).

After the solution of equation 3, it was noticed that the misclosure errors in the scan directions were quite high (about 30 pixels for the fore image and 27 pixels for the aft image) indicating a systematic bias in the scan direction. Table 2 gives the min, max and mean values for the disclosure errors for the fore and aft stereo images. After the bias is removed, the residual misclosure errors were reduced to a pixel level. Nevertheless, they still show a systematic trend. This may suggest that the RPCs have not been determined by a bundle adjustment solution. Figure 10 presents the scatter pattern of the misclosure errors for the fore and aft images respectively.

Table 2: *Misclosure (pixels) in scan direction (P), line direction (L), before the shift removal for the fore and aft stereo images*

Mean residual fore image (L)	Max residual fore image (L)	Min residual fore image (L)	Mean residual fore image (P)	Max residual fore image (P)	Min residual fore image (P)
-7E-5	+11E-4	-16E-4	30·78	31·5	29·9
Mean residual aft image (L)	Max residual aft image (L)	Min residual aft image (L)	Mean residual aft image (P)	Max residual aft image (P)	Min residual aft image (P)
7E-5	+17E-4	-11E-4	27·4	-26·7	-28·2

Table 3: *Misclosure (pixels) in scan direction (P), after the bias removal for the fore and aft stereo images*

Mean residual fore image (P)	Max residual fore image (P)	Min residual fore image (P)
8E-5	+0·8	-0·8
Mean residual aft image (P)	Max residual aft image (P)	Min residual aft image (P)
-9E-5	+0·7	-0·7

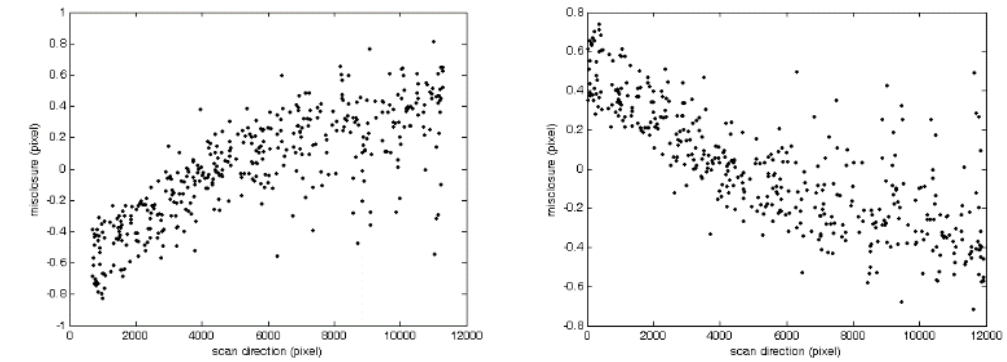

Figure 8: *Residual errors in the scan direction after the bias is removed for the fore (left) and aft (right) images*

After the solution of the RPC intersection, the UTM coordinates as optimum choice for the object coordinates discussed by Fraser et al., 2004, was adopted and, therefore, the calculated geodetic coordinates were transferred to the UTM coordinate system.

The 3D affine resection is then performed through which the affine coefficients are calculated. This stage is followed by the 3D affine intersection (equation 4) by which the 3D object coordinates are determined in the UTM coordinate system.

The following sub-sections present the accuracy results before and after the correction for the topographic influence:

3.1. Accuracy Evaluation before Eliminating the Effect of Topography

As mentioned in the previous sections, there are several factors that contribute to the deviation of the HRSI from the parallel projection geometry. The initial tests conducted on the P5 stereo-images are intended to highlight the total influence of all of these factors.

In the first stage, the dataset (A), which belongs to a highly mountainous terrain (see the Section: description of the datasets), used for the 3D affine accuracy evaluation. The residual discrepancies between the ground coordinates determined by the RPCs and the ground coordinates of the same points determined by 3D affine is determined based on equation 5. The rmse for E, N and h are given in Table 4. The residual error patterns for these parameters are presented in a kind of scatter diagram in Figures 9, 10 and 11 respectively. These scatter diagrams are very appropriate for revealing any trend in the residual errors.

Table 4: *rmse of the E, N, h residual errors for dataset A (without height and Earth curvature corrections)*

Rmse (E) – (meter)	Rmse (N) – (meter)	Rmse (h) – (meter)
4·67	1·77	4·53

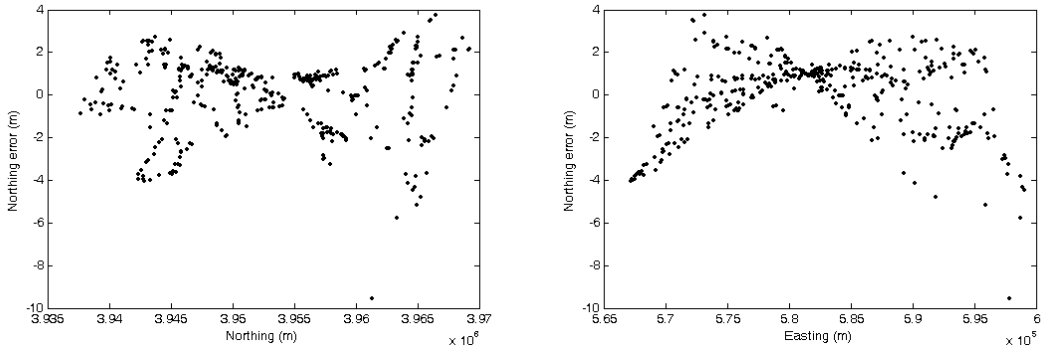

Figure 9: *(left): Northing error versus Northing, (right): Northing error versus Easting*

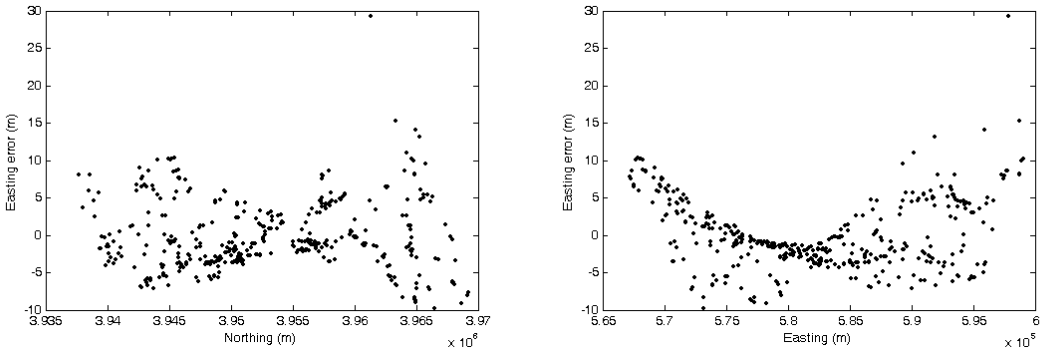

Figure 10: *(left): Easting error versus Northing, (right): Easting error versus Easting*

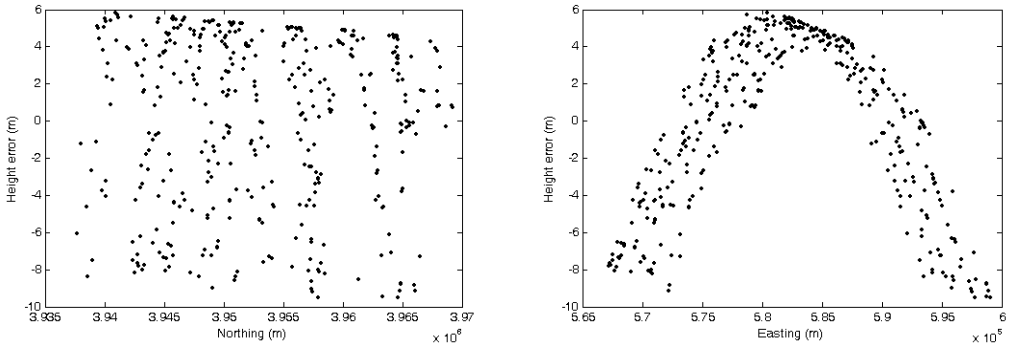

Figure 11: *(left): Height error versus Northing, (right): Height error versus Easting*

As the Figures indicate, the simple 3D affine is incapable to produce a good fit to the rational function in a highly mountainous terrain. This is, of course, in full agreement with the nature of the affine transformation. The main sources of errors in planimetry are due to the relief variations. As it was discussed earlier, the relief variation violates the parallel geometry in the scan line direction. This is clearly demonstrated in the scatter patterns presented in Figures 10(left & right). Nevertheless, Figures 9(left & right) also suggest that the relief variation has had some impact, although with a lower magnitude, on the line direction.

Figure 11(right) indicates a nearly curved pattern for the height discrepancies. This clearly suggests that the terrain topography does not play a decisive role on the height accuracy and this is the Earth curvature that dominantly affects the height residuals.

To further indicate the influence of topography on the performance of the 3D affine transformation, dataset B belonging to a hilly area is used. The results are presented in Table 5 and Figure 12 respectively. As can be seen from the Table and the residual scatter patterns, the accuracy improvement is clear. The max/min errors are less than a meter for all of the points indicating a sub-pixel fitting accuracy in the image space. This, of course, proves the considerable influence of the terrain height fluctuation in the fitting accuracy of the 3D affine transformation. It is important to notice that although rmse values are considerably reduced in dataset B as compared to the first dataset, the systematic trend in the E and N residual errors still is detectable which indicates that the influence of the height variations in the dataset B is still significant.

As Table 5 indicates, the errors in height have not been improved as compared to the dataset A. This is due to the fact that the errors due to the Earth curvature have remained intact.

Table 5: *Rmse of the E, N, h residual error for dataset B (without height and Earth curvature corrections)*

Rmse (E) – (meter)	Rmse (N) – (meter)	Rmse (h) – (meter)
0.35	0.28	5.17

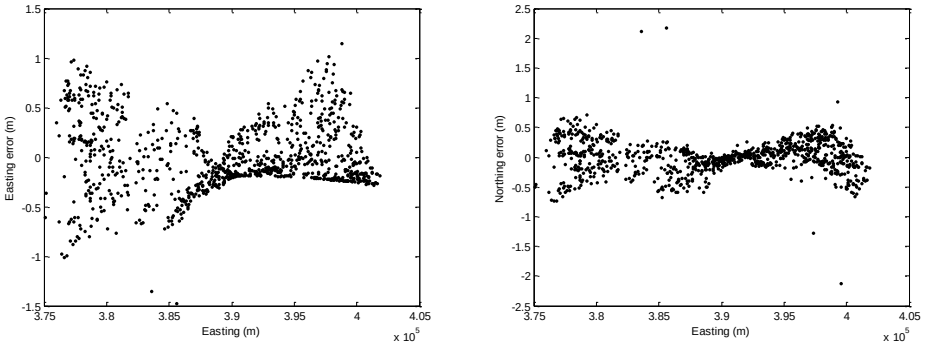

Figure 12: *N and E residual errors (hilly terrain, dataset B)*

3.2. Accuracy Evaluation after Eliminating the Effect of Topography

The next step involves the elimination of the influence of the terrain topography. This is achieved via the familiar perspective to parallel transformation, (Fraser and Yamakava, 2004):

$$y' = \frac{y}{1 - \frac{y}{f}\tan\omega} \pm \left[\tan(\omega + \alpha) - \tan\omega\right]\Delta Z \cos\omega$$

where y and y' are the pixel coordinates in the scan direction before and after the perspective to parallel transformation; ΔZ is the height variations brought into a scale close to the image scale; ω is the roll angle; α is the angle between the camera optical axis and the line connecting each pixel to the perspective centre and f is the camera focal length. However, as the roll angle, for the along track stereo images is nearly zero, the perspective to parallel transformation equation reduces to:

$$\Delta y = \Delta Z \tan\alpha \qquad (7)$$

Where Δy is the perspective to parallel corrections applied to the pixel coordinates in the scan direction.

After applying Equation 7 to the measured image coordinates in the fore and aft images, the affine space resection followed by the affine space intersection is carried out and the ground points are generated. The rmse for E and N are presented in Table 6. The planimetric accuracy improvements as compared to the results obtained before PTP can be clearly seen in Table 6. However, as expected, the rmse value for the height discrepancies has not changed, i.e. rmse of heights are 4·51 and 4·53 meters before and after applying PTP respectively. This again shows that the height accuracy is less sensitive to the terrain topography.

Table 4: *Rmse of the E, N, h residual error for dataset A, before and after perspective to parallel transformation*

Rmse (E) – (mster) (before PTP)	Rmse (N) – (mster) (before PTP)	Rmse (E) – (mster) (after PTP)	Rmse (N) – (mster) (after PTP)
4.67	1.77	0.34	0.86

As it was mentioned earlier, the scatter diagram should be checked to detect the possible trends in the residual errors. Figures 13 and 14 show the scatter patterns of the errors in planimetry.

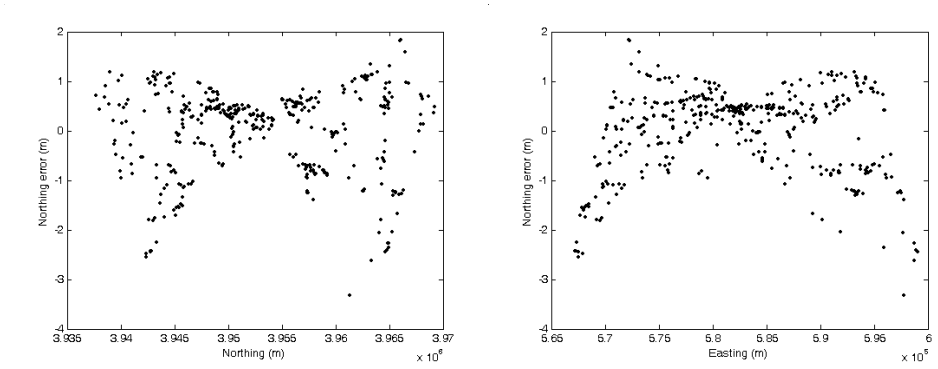

Figure 13: *(left): N error versus N, (right): E error versus E, (dataset A)*

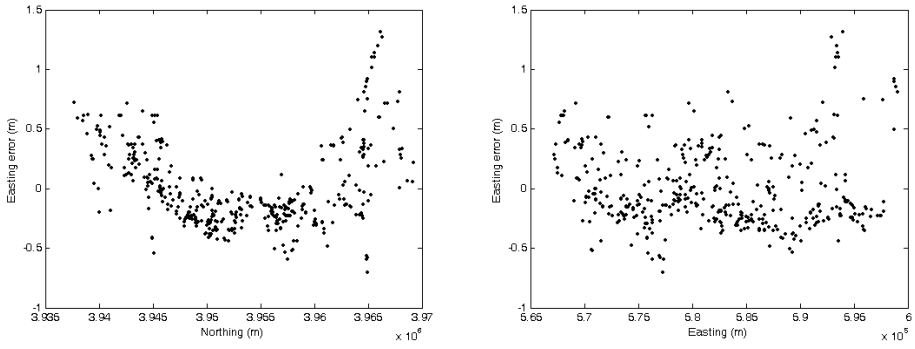

Figure 14: *(left): E error versus N, (right): E error versus E, (dataset A)*

3.3. Issues Related to the Earth Curvature

It was demonstrated in the preceding sections, that the displacements due to the Earth curvature on the object coordinates are inevitable when the 3D affine transformation is at issue. It was also demonstrated that this displacement is dominant over the height coordinates.

To remove the displacement effect of the Earth curvature, two different approaches have been adopted, namely, image space and object space solutions: In the first approach, the displacements due to the Earth curvature are formulated in the image space. To model the image point displacement due to the Earth curvature, it is assumed that the imaging geometry for each scan line is identical to the diagram depicted in Figure 15.

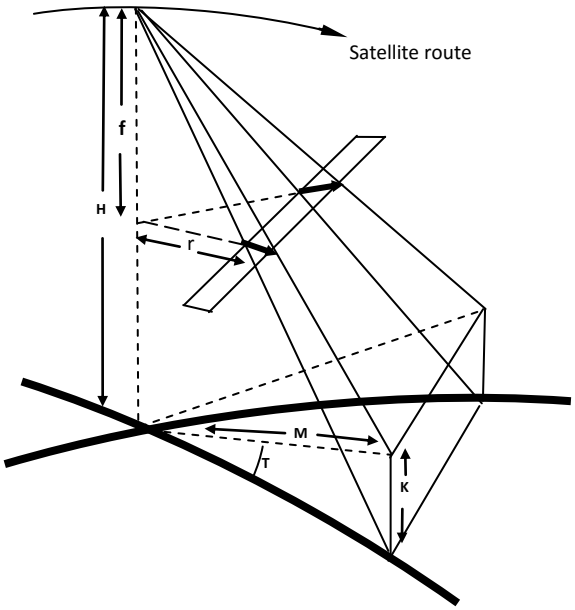

Figure 15: *Image displacements due to Earth Curvature along the scan lines*

With reference to Figure 16, it can be shown that the following relation holds true:

$$K = R - R\cos(2T) \qquad (8)$$

Where *R* is the Earth radius; *K* is the vertical displacement of a point on the Earth surface and the planar surface formed on the object space by the affine transformation. This surface is indicated in Figure 15 by the dashed lines that are tangent to the Earth surface at the ground nadir point; and *T* is the angle between the tangent to the Earth surface and the planar surface generated by the affine transformation. This angle may be expressed as:

$$\sin(2T) = \frac{M}{R} \qquad (9)$$

Where *M* is the horizontal distance between the object point and the ground nadir point. From Equations 8 and 9 it can be deduced that:

$$K = 2R\frac{M^2}{4R^2} = \frac{M^2}{2R} \qquad (10)$$

M may be expressed as a function of the radial distance, *r*, from the image nadir point:

$$M = r * H / f \qquad (11)$$

Where *H* is the satellite flying height and *f* is obtained via: $f'*\cos\theta$ in which *f'* and θ are the camera focal length and the satellite pitch angle respectively. By replacing Equation 11 in 10, we get:

$$K = \frac{r^2 \frac{H^2}{f^2}}{2R}$$

The image displacement, Δr, due to the value of *K* can then be expressed as:

$$\Delta r = \frac{r^3 H^2}{2Rf^2} \qquad (12)$$

This relation is identical to the classical formulation in photogrammetry for the Earth curvature for frame photography. Based on the equation 12, the theoretical displacement is determined and is presented in Figure 16.

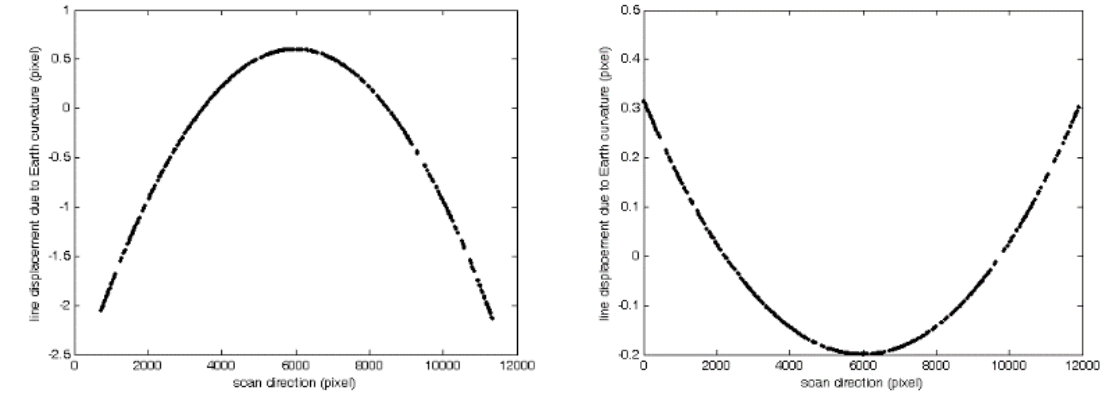

Figure 16: *Image displacement due to Earth Curvature evaluated via equation 12, (left): fore image, (right): aft image*

The theoretical formulation given by equation 12 is validated by the actual determination of the pixel displacements due to the Earth curvature for the dataset (A). This is achieved by the inverse solution of the affine transformation. That is, the object points are transformed to the image space via inverse affine parameters. The object coordinates in this case are the E, N values already computed by the affine intersection. However, the height values for each object point are replaced by the heights generated by the RPCs that are free from the Earth curvature displacements. The image space residuals due to the Earth curvature are then the differences between the transformed image coordinates and the originally measured image points. Figure 17 show these displacements for the fore and aft images respectively. As can be seen, the image coordinates distortion curves are in the sample direction and they are in conformity with the scatter diagrams depicted in Figure 16. From these figures it can be also seen that because of the smaller oblique viewing angle, the amplitude of the image displacement due to the Earth curvature in aft image is smaller than that of the fore image.

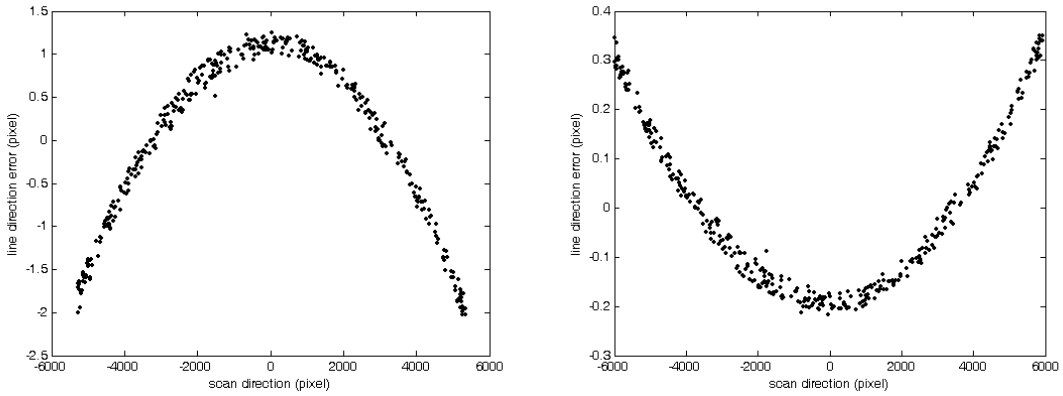

Figure 17: *line direction displacement due to the Earth curvature, (left) fore scene, (right) aft scene*

The second approach formulates the Earth curvature directly on the 3D affine generated height values on the object space. This alternative approach entails the direct utilization of Equation 10, in which the value of *K* is taken to directly represent the height displacement due to the Earth curvature. The value of *M* in Equation 10 is interpreted in this case as the shortest distance of the object points to the satellite ground track (SGT). To implement this approach, the SGT is determined. This is achieved by transferring the middle pixels of the images to the object space. Alternatively the SGT may be determined via the satellite heading from the metadata. After the computation of the shortest distance to the SGT for all generated object points, the Earth curvature is computed based on Equation 10. Figure 18 presents the residual height scatter diagram after removing the Earth curvature effect. The RMSE of the residual height errors has been reduced to 0·41 meter which is significantly better than 4·53 meters before eliminating the Earth curvature effect. Nevertheless, Figure 18 shows a systematic trend in the Northing direction. This may suggest that the height errors are also proportional to the direction of the satellite movement in which the satellite undergoes a slight altitude variation. The inclusion of the term (*NZ*) in the affine model, therefore, may improve the result. This is a matter for further investigation.

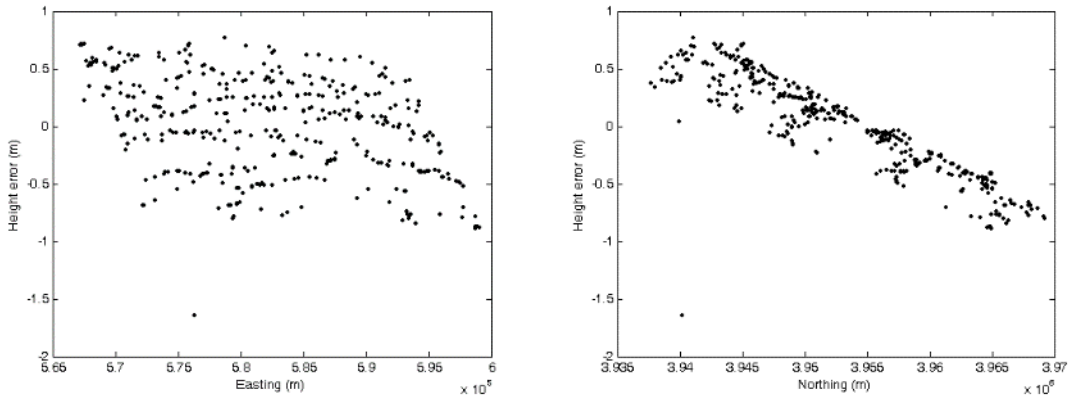

Figure 18: *(left): height residuals versus Easting, (right): height residuals versus Northing, after the elimination of the Earth curvature effect*

The overall achieved fitting accuracy of the 3D affine transformation before and after height correction and Earth curvature removal for comparison is given in Table 7.

Table 7: *The overall accuracy figures for dataset (A) and (B) before and after applying the height and earth curvature corrections*

	Before corrections applied			After corrections applied		
	δE (m) - min/max	δN (m) - min/max	δh (m) - min/max	δE (m) - min/max	δN (m) - min/max	δh (m) - min/max
Dataset(A)	0·01/29	0·002/9·5	0·08/9·6	8E-4/1·4	1E-4/3·3	5E-4/2·4
Dataset(B)	1E-3/1	1E-5/0·6	1E-3/20	2E-4/1·07	6E-4/0·8	3E-5/0·3

The section that follows summarizes the whole theme of the paper and draws the necessary conclusions.

4. Concluding Remarks

Based on the results and the discussions presented in the preceding chapters, the following conclusions may be made:

(1) Affine transformation can indeed approach the accuracy of the rational function with sub-pixel level.
(2) The accuracy results deteriorate with increase in the camera field of view and increase in the terrain relief undulation.
(3) Based on the theoretical concepts and the conducted tests, it seems unlikely that the pure 3D affine model can generate data with accuracies equal to the RPCs. The theoretical justification of this statement, moreover, lies in the fact that even in the absence of the errors such as the attitude and altitude and relief variations, still Earth curvature intervenes in the computational process.
(4) The height variation in mountainous terrain does not seem to solely affect the scan direction. The conducted tests indicate that the line direction also receives some influence from the terrain relief undulation.
(5) Even if the effect of the height variation by PTP transformation is eliminated and the earth curvature removed, still some trends, though very marginal, can be observed in the scatter pattern.
(6) The RMSE and max/min errors cannot adequately indicate the quality of the residual errors. In fact, this is the scatter pattern for the point clouds that indicates the presence or the absence of the trends in the final output and the success of the 3D affine transformation cannot be realistically judged with small and uneven distribution of the GCPs.

References

Dadrass, F. and Azizi, A. *The Affine Projection Model as a Tool for Rapid Geo-Coding of IRS-P5 Satellite Imagery.* The International Archives of the Photogrammetry, Remote Sensing and Spatial Information Sciences. 2008. 37 (B4) 1317-1322.

Dial, G. and Grodecki, J. *RPC Replacement Camera Models.* International Archives of Photogrammetry, Remote Sensing and Spatial Information Sciences. 2005. 34; Part XXX.

Elashmawy, N., Elmanadili, Y., and Barakat, H., 2005. *Comparative Analysis and Evaluation of Various Mathematical Models for Stereo IKONOS Satellite Images.* FIG Working Week and Gsdi-8, Cairo, Egypt. 1-16.

Frase, C.S. and Hanley, H.B. *Bias Compensation in Rational Functions for IKONOS Satellite Imagery*. Photogrammetric Engineering and Remote Sensing. 2003. 69 (1) 53-57.

Fraser, C.S. and Yamakawa, T. *Insights into the Affine Model for Satellite Sensor Orientation*. ISPRS Journal of Photogrammetry and Remote Sensing. 2004. 58 (5-6) 275-288.

Grodecki, Jacek, 2001: *IKONOS Stereo Feature Extraction-RPC Approach*. Proceedings of ASPRS 2001 Conference, St. Louis, April 23-27. 7.

Grodecki, J. and Dial, G. *Block Adjustment of High Resolution Satellite Images Described by Rational Polynomials*. Photogrammetric Engineering and Remote Sensing. 2003. 69 (1) 59-68.

Grodecki, J., Dial, G., and Lutes, J., 2004: *Mathematical Model for 3d Feature Extraction from Multiple Satellite Images described by RPCs.* ASPRS Annual Conference Proceedings May 2004, Denver, Colorado.

Hanley, H.B. and Fraser, C.S. *Sensor Orientation for High-Resolution Satellite Imagery: Further Insights into Bias-Compensated RPCs.* International Archives of the Photogrammetry, Remote Sensing and Spatial Information Sciences. 2004. 35 (B1) 24-29.

Morgan, M., 2004: *Epipolar Resampling of Linear Array Scanner Scenes*. Ph.D. Dissertation, Department of Geomatics Engineering, University of Calgary, Canada.

Morgan, M., Kim, K., Jeong, S., and Habib, A., 2004: *Indirect Epipolar Resampling of Scenes using Parallel Projection Modeling of Linear Array Scanners.* XXth Congress of ISPRS. July 2004.

Okamoto, A., Fraser, C., Hattori, S., Hasegawa, H., and Ono, T. *An Alternative Approach to the Triangulation of Spot Imagery.* International Archives of Photogrammetry and Remote Sensing. 1998. 32 (B4) 457-462.

Tao, C.V. and Hu, Y. *A Comprehensive Study of the Rational Function Model for Photogrammetric Processing.* Photogrammetric Engineering and Remote Sensing. 2001. 67 (12) 1347-1357.

Valadan Zoej, M.J. and Petrie, G. *Mathematical Modeling and Accuracy Testing of Spot Level 1b Stereo-Pairs.* Photogrammetric Record. 1998. 16 (91) 67-82.

Willneff, J., Weser, T., Rottensteiner, F., and Fraser, C.S. *Precise Georefrencing of Cartosat Imagery via Different Orientation Models.* The International Archives of the Photogrammetry, Remote Sensing and Spatial Information Sciences. 2008. 37 (B1) 1287-1294.